Aggregation of growing crystals in suspension: II. Poiseuille flow crystalliser

Kate Pitt, Michael J. Hounslow*

Department of Chemical and Biological Engineering, The University of Sheffield, Sheffield S1 3JD, UK

HIGHLIGHTS

- The Poiseuille Flow Crystallizer (PFC) characterises fluid flow field with great accuracy.
- The PFC acts as a differential reactor and changes in the size distribution evidence aggregation.
- We can deconvolute averaged aggregation efficiency values over flow field to obtain point values.
- For calcium oxalate (COM) the rate limiting process is rupture under simple tension.
- For COM we deduce the unknown materials properties that determine the tendency to aggregate.

GRAPHICAL ABSTRACT
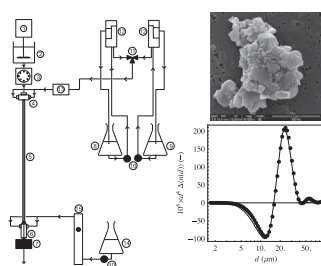
ABSTRACT

We describe the design and operation of a Poiseuille Flow Crystalliser (PFC) that allows direct exploration of the effect of hydrodynamic and physico-chemical conditions on the aggregation of crystals growing in suspension. The PFC operates as a differential reactor where changes between inlet and outlet are small enough not to change the rate, but large enough to be measureable. Automatically measured changes in size distribution yield very clear quantitative evidence of aggregation. We use these data to explore the three open questions of Hounslow et al. (2013) and show how to average underlying point aggregation kinetics over a whole vessel and how to extract point data from average data. We introduce the critical aggregate size, D, as the particle size that at the average shear rate has a Mumtaz number, $M=1$, and so disruptive forces are in balance with the strength of growing bridges.

In a study of rounded calcium oxalate monohydrate particles we show that values of D can readily be determined by fitting the change in size distribution in the PFC. We are able to discriminate among candidate models relating aggregation efficiency to M by means of an empirical fitting investigation and by directly determining the aggregation efficiency – both averaged and un-averaged for the vessel. We conclude that aggregate rupture happens under simple tension and that the effective average size of two colliding particles is their geometric mean.

D^2 is predicted and observed to be directly proportional to the ratio of crystal growth rate to flow rate squared. We demonstrate that no attractive or repulsive inter-particle forces are active in aiding or retarding aggregation in this system. The constant of proportionality from these results allows the material property controlling aggregation – the product of yield strength and a geometric factor with dimensions of length – to be determined as $L^*\sigma_Y = 1.35 \pm 0.01$ Nm^{-1}.

© 2014 The Authors. Published by Elsevier Ltd. This is an open access article under the CC BY license (http://creativecommons.org/licenses/by/3.0/).

* Corresponding author.
  E-mail address: m.j.hounslow@sheffield.ac.uk (M.J. Hounslow).

1. Introduction

In the first paper of this series (Hounslow et al., 2013) – henceforth to be referred to as Part I – we developed Mumtaz's theory (Hounslow et al., 2001) for the rate of aggregation of growing crystals in suspension in the context of a thorough literature survey. In what follows, we briefly summarise the elements of that theory. It is well established that when crystals are present in a supersaturated solution, relative motion will induce collisions and that some of those collisions will result in permanent attachment of the colliding crystal to each other. It is further well established that over a range of sizes and operating conditions the relative motion is induced by fluid shear so the collision rate can be described by

$$r_C = C_0 N_I N_{II} \tag{1}$$

where N is the number of particles per unit volume in suspension of "type" (e.g. size) I or II involved in a collision. C_0 is Smoluchowski's shear kernel (Smoluchowski, 1917):

$$C_0 = \frac{\dot{\gamma}}{6}(d_I + d_{II})^3 \tag{2}$$

where $\dot{\gamma}$ is the local shear rate or velocity gradient, and d_I and d_{II} are the particle diameters. We refer to particles in this work to mean any single, separate crystal or aggregate of crystals.

Since not all collisions result in the formation of an aggregate, the aggregation rate, r_A, is in general less than the collision rate, r_C. We identify the fraction that are "successful" in forming an aggregate as the efficiency:

$$\psi = r_A / r_C \tag{3}$$

It follows that an aggregation rate constant, or kernel, β_0, can be related to the collision rate constant as

$$\beta_0 = \psi C_0 = \psi \frac{\dot{\gamma}}{6}(d_I + d_{II})^3 \tag{4}$$

We have recently shown from first principles in Part I that efficiency is expected to depend only on a dimensionless parameter we term the Mumtaz number:

$$M = \frac{\sigma_Y L^* G}{\dot{\gamma}^2 \mu d_{eq}^2} \tag{5}$$

where d_{eq} is the equivalent diameter of two colliding particles, introduced in Part I, based on the geometric mean size $\overline{d}_g$

$$d_{eq} = q\overline{d}_g = q\sqrt{d_I d_{II}} \tag{6}$$

and q is the mean size correction factor. σ_y is the yield strength of the material cementing the colliding particles together, L^* is a geometric factor combining the length of a linear feature where initial contact is made between the particles and the geometry of the collision, G is the linear rate of growth of the crystals as a consequence of supersaturation and μ is the dynamic viscosity of the solution.

The dependence of ψ on M depends on the mechanism of rupture for the newly formed neck, or bridge, between the colliding particles. We hypothesised that failure might occur simply through tension or through shear and tension combined. The combination of shear and tension might be according to Tresca's or von Mise's criteria, however the curves relating ψ to M for these criteria are the same with a small shift to larger values of M for Tresca's criterion. For that reason if a model derived from Tresca's criterion could be fitted to the data, then so too could one based on von Mise's.

The above description of collisions, rate constants, efficiency and Mumtaz number all apply at a point in space only since many of the system properties, especially shear rate, should be expected to vary with position. In any experimental study, observations can only be made that are averaged in some way over space, and usually over a whole vessel. We have had considerable success e.g. Pitt et al. (2012). In using an average rate constant and efficiency

which, in turn, we relate to an average Mumtaz number. The nature of that averaging has been largely arbitrary since no underlying knowledge of the distribution of shear rate was available. As a consequence, only a qualitative connection between the theoretical point kinetics and the observed average kinetics has been possible. Exceptions to this limitation can be found in the work of (Hollander et al., 2002; Ilievski et al., 2001) where in both cases a Couette device is used in batch mode to create a readily quantifiable flow field. In both cases, however, either turbulent flow must be used or it must be recognised that gravity will cause particles to settle to the walls of the vessel. By contrast, Mumtaz and Hounslow (2000) used a vertical capillary in which laminar, or Poiseuille, flow could be induced so creating a Poiseuille Flow Crystalliser (PFC) operating in continuous mode negating the influence of gravity.

The purpose of the present paper is to

- report the development of a PFC capable of automated high quality measurements
- develop a rigorous approach linking theoretical point kinetics and theoretical averaged kinetics
- test the theoretical kinetics previously reported
- develop techniques for deducing point kinetics from experimental average kinetics

In so doing, we seek to address the three open questions of Part I:

- which failure mode is appropriate?
- what value does $L^* \sigma_Y$ take for a given material?
- how should these point kinetics be averaged over a whole vessel?

2. Equipment and method

In this paper we describe how the well-known characteristics of Poiseuille flow may be exploited in a study of aggregation of calcium oxalate monohydrate (COM) during precipitation using the Poiseuille Flow Crystalliser (PFC). The PFC was operated at steady state with a pre-mixed feed of particles and solutions fed at the top of the crystalliser and the effluent at the bottom of the crystalliser analysed on-line using a particle counter and sizer.

2.1. Equipment

#### 2.1.1. Poiseuille flow crystalliser

A schematic diagram is shown in Fig. 1. The PFC consists of a vertically orientated glass capillary tube (length 1.5 m, outer diameter=5 mm, nominal inner diameter=1 mm) supplied by Dixon Glass Ltd., Kent, UK, with associated pumps (Iwaki MD-10) and storage reservoirs. The seed suspension and solutions (either saturated or metastable) were fed into the capillary tube via a mixing adaptor shown in Fig. 2. The two horizontally opposed arms receive solution from head tanks via a flow controller (Bronkhorst Liqui Flow Controller IP-40, 0.02–1 ml/min). The seeds are introduced via a peristaltic pump (Pharmacia Fine Chemicals, P-1) from above. The mixed solution and seeds then pass vertically down the capillary tube. Capillary flow rates ranged from 0.5 ml/min to 1 ml/ml. Capillary seed concentrations ranged from 0.20 kg m^{-3} to 1.0 kg m^{-3}.

2.1.2. Particle size analysis

All crystal size distributions and number data were obtained using an Accusizer 780 Optical Particle Sizer (PSS.NICOMP Particle Sizing Systems, Santa Barbara, US). Prior to particle analysis, the
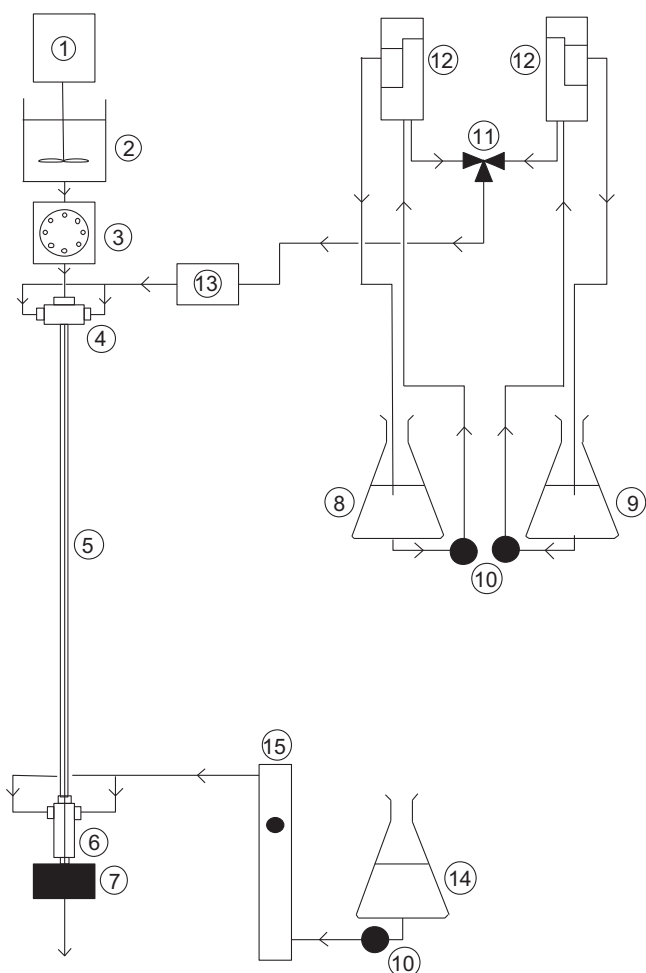
Fig. 1. Schematic diagram of the Poiseuille-flow crystalliser showing (1) overhead stirrer; (2) seed reservoir; (3) peristaltic pump; (4) upper mixing adaptor; (5) glass capillary; (6) lower mixing adaptor; (7) Accusizer sensor; (8) saturated solution reservoir; (9) metastable solution reservoir; (10) centrifugal pumps; (11) three-way valve; (12) head tanks; (13) flow controller; (14) dilution saturated solution reservoir; and (15) flowmeter.
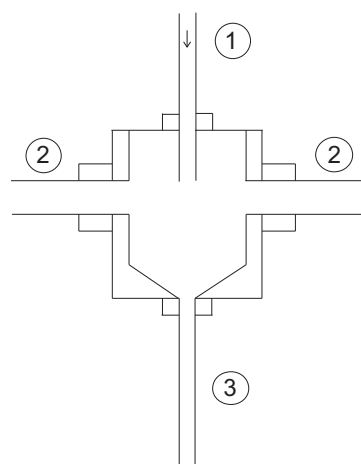
Fig. 2. Schematic cross-section of the upper mixing adaptor showing: (1) direction of seed flow; (2) horizontally opposed solution inlets; (3) glass capillary.

mixed solution and seed was diluted with saturated solution in a lower mixing adaptor fed via a pump and flow metre (Cole Parmer 150 mm-Correlated Flowmeter, 0–84 ml/min flow rate). This was

necessary to meet the optimal particle concentration operating conditions of the Accusizer.

2.2. Materials

2.2.1. Solutions

All chemicals used in the preparation of the solutions were of analytical grade. The water used was distilled, then deionised and filtered using an Elga Classic DI MK2 Purification system with a 0.2 μm filter.

Two types of solutions were employed: metastable (supersaturated) and saturated.

A range of metastable solutions were prepared having an initial supersaturation ranging from $S-1=1.65$ to 3.10 where relative supersaturation is

$$S = \sqrt{\frac{\gamma_\pm^2 \left[\text{Ca}^{2+}\right]\left[\text{Ox}^{2-}\right]}{K_{sp}}} \qquad (7)$$

as described in Pitt et al. (2012).

Growth rates for COM crystals can be calculated from supersaturation using the relationships presented in Pitt et al. (2012).

In these solutions, the calcium ions are provided by $CaCl_2$ and the oxalate ions by $Na_2C_2O_4$. The solutions were made up to an ionic strength of 0.16 M by the addition of NaCl. The final pH of the solutions was 6.0.

Saturated solutions were prepared by adding solid COM (Alfa Aesar) to a saline solution of approximately 0.16 M, magnetically stirred for a minimum of 24 h and filtered using 0.2 μm pore size cellulose nitrate membrane filter papers (Whatmann, UK).

2.2.2. Seed suspensions

Seed suspensions consisting of crystallographically poorly-defined COM crystals were prepared by wet grinding 1 g of commercially-supplied COM (Alfa Aesar) in a mortar. These crystals were then suspended in a metastable solution prepared as described below ($S-1=1.65$). This seed suspension was stored at 21 °C in a reservoir at the top of the PFC and stirred using an overhead stirrer. Suspensions were aged for a minimum of one week before use. The mean size of the individual crystals was approximately one micron, and the mean size of the seed aggregates was typically 8μm as measured by an Accusizer 780 Optical Particle Sizer (PSS.NICOMP Systems, Santa Barbara, US). Fig. 3 shows that the suspension consisted of aggregates of COM. We refer to these seeds as *rounded* COM.

2.2.3. Methods

After cleaning and flushing, saturated solution was fed to the PFC. Crystal size distributions were measured by the Accusizer to check for background particles. Then the seed suspension was introduced into the mixer via the persistalic pump and the solution flow rate was adjusted to the desired value. After steady state was reached crystal size distributions were measured by the Accusizer. Typically, a minimum of ten size distributions were measured for each working condition. Size distributions measured in this way in saturated solution are found to be the same as those entering the capillary and will, for brevity, be referred to as inlet distributions.

Having determined the inlet distribution, the solution feed was switched from saturated to metastable solution and again a minimum of ten crystal size distributions were measured at steady state. The distributions measured in metastable solution are referred to as outlet distributions.

The solution feed was eventually switched back to saturated solution, and further crystal size distributions measured to ensure that the inlet distribution had not changed.
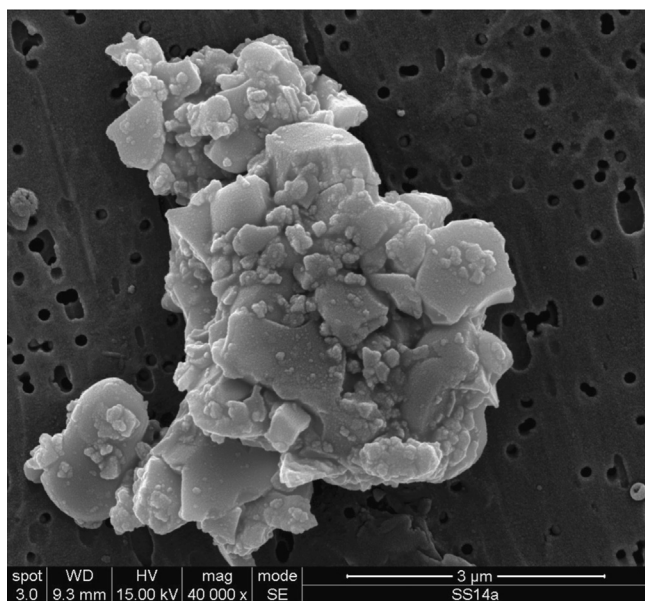
Fig. 3. SEM image of aggregates taken from a seed suspension of *rounded* COM.

Fig. 4. Breakthrough times measured for solids (●) and solute (○) in the PFC. The line corresponds to Eq. (9).

Fig. 5. The step response to a change in seed flow rate presented as a cumulative residence time distribution. The legend shows the capillary flow rate in ml min^{-1} and the line is Eq. (8).

The working conditions under investigation were capillary seed concentration in the range 0.20 kg m^{-3}–1.0 kg m^{-3}, capillary flow rate in the range 0.5–1.0 ml/min and the supersaturation of the metastable solution, $S-1=1.65$ to 3.10. All experiments were carried out at 21 °C.

2.3. Characterising the PFC

It is of importance to this work that the particles present are known to follow the fluid streamlines and thus have the well known parabolic distribution of velocities. Confirmation that this is so was obtained by measurement of the residence time distributions (RTDs) for solids and the dissolved solute.

According to Danckwerts (1953), the RTD in Poiseuille flow is given by

$$F(t) = \begin{cases} 0 & t \leq t_0 \\ 1-(t_0/t)^2 & t > t_0 \end{cases} \qquad (8)$$

where the breakthrough time, t_0, is half the mean residence time and can be related to volumetric flow rate, Q, and the geometry of the capillary by

$$t_0 = \frac{\pi L R^2}{2Q} \qquad (9)$$

where L is the length of the capillary tube and R is the radius of the capillary.

Two techniques were used to determine the breakthrough time experimentally for a variety of flow rates. First, the time for the seed to travel down the length of the capillary tube over a range of flow rates was recorded using the Accusizer to detect the presence of solids. In the second technique, the seed suspension was replaced by a 3 M NaCl solution and the time taken for the solution to travel the length of the tube was detected by conductivity measurement.

Results for both techniques are shown in Fig. 4 and demonstrate that the solids and the solute have indistinguishable breakthrough times and that both are inversely proportional to flow rate as described in Eq. (9). From the slope of the line in Fig. 4 it is possible to determine the radius of the capillary as $R=0.371 \pm 0.002$ mm.
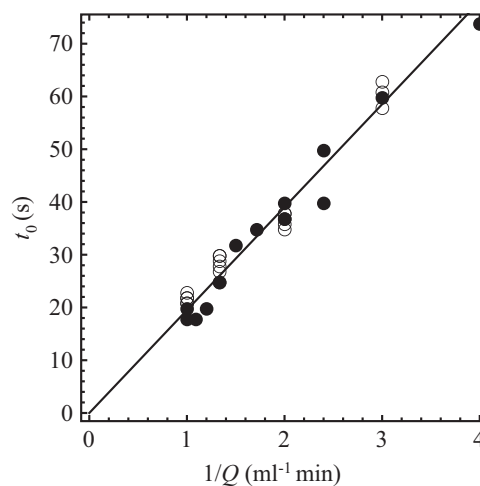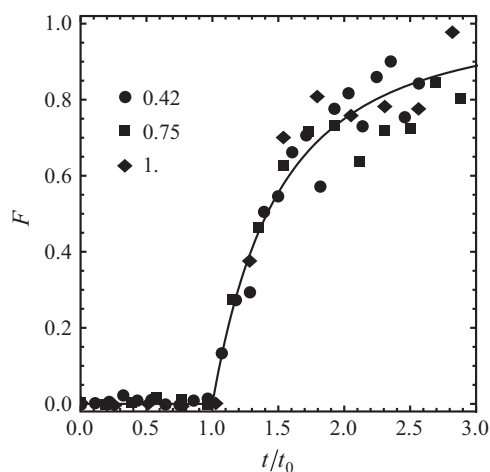
To further check that the solids follow the expected velocity distribution, the step response to a change in seeds flow rate was recorded for three different capillary flow rates. The results shown in Fig. 5, calculated using the capillary radius reported above and no further fitted parameter, are compelling evidence that the solids are uniformly distributed across the capillary and follow the expected fluid streamlines and velocity distribution.

3. Typical data

Typical data obtained from the PFC are shown in Fig. 6 for an experiment conducted at a flow rate of 0.75 ml min^{-1} and a supersaturation of $S-1=2.68$ using well-defined seeds.

In Fig. 6(a) the data are presented as a number distribution – with the area under the curve corresponding to the number of particles per unit volume in a size range. It is clear that there is a larger number of particles flowing in than out (the area under the curve reduces) and that the particles leaving the PFC are larger (the curve moves to the right).

In Fig. 6(b) the data are presented as a volume density – the area corresponding to a volume of particles per volume of suspension. In this case, the move to larger sizes is still apparent, but there is a slight increase in area under the curve.
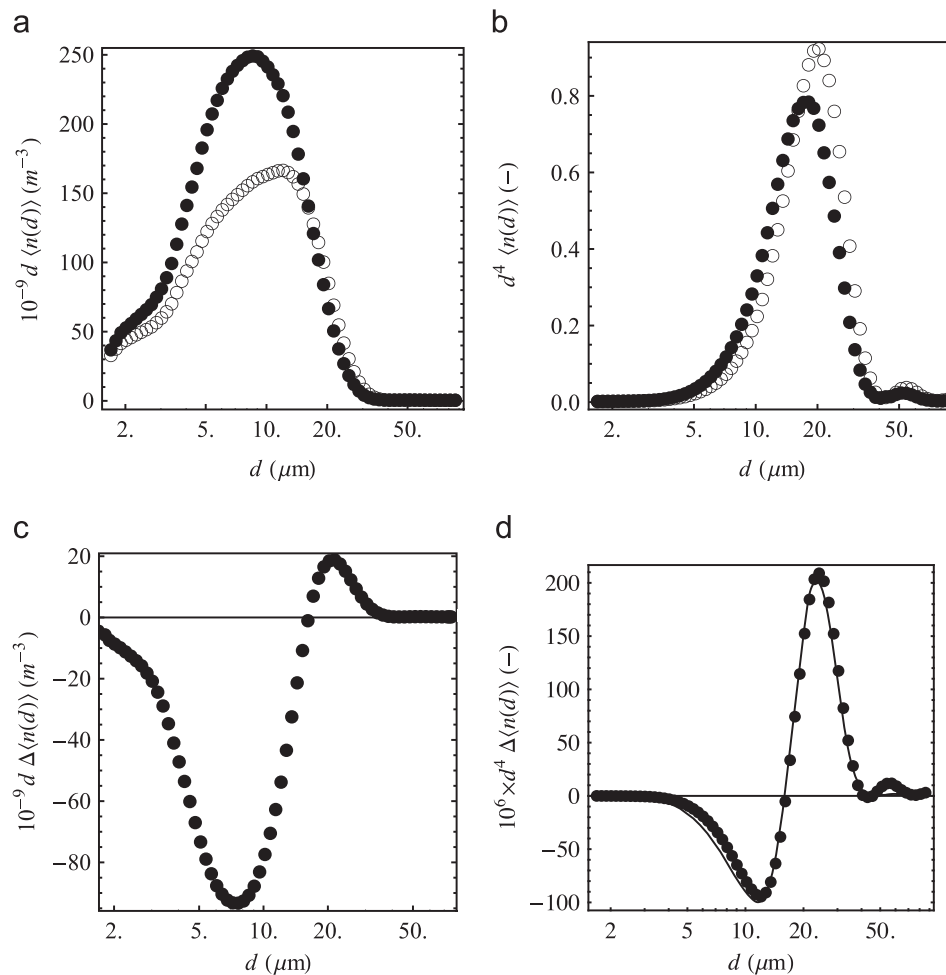
Fig. 6. Example distributions flowing into (●) and out of (○) the PFC as (a) a number density, (b) a volume density, (c) a change in number density and (d) as a change in volume density. The line in (d) corresponds to a best fit with $D=10.2$ μm with failure under tension with $q=1$.

These results together are entirely consistent with a process dominated by aggregation (number decrease, size increase, volume conserved) in the presence of a small amount of growth (numbers conserved, size increases, volume increases).

In Fig. 6(c) and (d) the number and volume distributions are shown as the change, or difference (out–in). Negative regions of the functions correspond to a reduction (in number or volume) at that size and positive regions an increase. It is apparent that the results in this different form give a clear signal of the extent of the rate processes and the particle size at which their impact occurs.

In what follows we develop a population balance model that relates the kinetic parameters, and particularly the aggregation efficiency, to data of the form shown in Fig. 6.

4. Theory

In the PFC, collision rates and aggregation efficiencies vary with position because the shear rate, $\dot{\gamma}$, and so M, vary with position. We can, however, only make measurement of the size distributions entering and leaving the crystalliser. In fact these distributions are *mixing–cup* averages at the inlet and outlet, since the actual distributions might vary across the width of the capillary.

4.1. Spatial averaging over the vessel

It is apparent that the change in particle size distribution (PSD) should contain considerable, size–resolved information about the

aggregation rate constant and so the efficiency. In order to extract that information we need to address the third open question of Part I:

"how should these point kinetics be averaged over a whole vessel?"

The velocity in the PFC is given in cylindrical coordinates as

$$\mathbf{u} = (u_r, u_\theta, u_z) = \left(0, 0, U_0\left(1-(r/R)^2\right)\right) \quad (10)$$

so at any point the shear rate is

$$\dot{\gamma} = \frac{2rU_0}{R^2} \quad (11)$$

For any function of radial position $f(r)$ we can define two useful averages for the whole PFC:

the in–situ average $\quad \bar{f} = \frac{2}{R^2}\int_0^R rf(r)\,dr \quad (12)$

and a mixing–cup average

and a mixing–cup average $\quad \langle f \rangle = \frac{\int_0^R rf(r)u_z(r)\,dr}{\int_0^R ru_z(r)dr} = \frac{4}{R^2U_0}\int_0^R rf(r)u_z(r)\,dr \quad (13)$

Two in–situ averages are particularly useful:

velocity $\quad \bar{u}_z = \bar{u} = \frac{U_0}{2} \quad (14)$

shear rate $\quad \bar{\gamma} = \dfrac{4U_0}{3R}$ (15)

The flow rate, Q, is related to the centre–line velocity, U_0, by

$$Q = \pi R^2 \bar{u} = \pi R^2 \frac{U_0}{2}$$ (16)

4.2. Population balance

At a point (r,θ,z) the size distribution is described by a number density, $n(d,r,z)$, where we assume that there is no dependence on θ. At steady state, the Population Balance Equation, PBE, (Randolph and Larson, 1988) gives

$$G\frac{\partial n(d,r,z)}{\partial d} + u_z(r)\frac{\partial n(d,r,z)}{\partial z} = S(d,r,z)$$ (17)

where the source term due to aggregation is

$$S(d,r,z) = \frac{d}{2}\int_{d'^3 + d''^3 = d^3} \frac{\beta(d',d'',r,z)n(d'',r,z)n(d',r,z)}{d''^2}dd' - n(d,r,z)$$
$$\int_0^\infty \beta(d,d',r,z)n(d'r,z)dd'$$ (18)

In–situ averaging of the PBE gives

$$G\frac{\partial \bar{n}(d,z)}{\partial d} + \bar{u}\frac{\partial \langle n(d,z)\rangle}{\partial z} = \bar{S}(d,z)$$ (19)

We make the differential reactor assumption where we assume that n varies little with z, so that $\bar{n}(d,z) = \langle n(d,z)\rangle = n(d)$, $\frac{\partial \langle n(d,z)\rangle}{dz} = \frac{\Delta\langle n(d)\rangle}{Z}$ so the PBE becomes

$$G\frac{\partial n(d)}{\partial d} + \frac{\bar{u}}{Z}\Delta\langle n(d)\rangle = \bar{S}(d)$$ (20)

Noting $\bar{u}/Z = \bar{t}$, the average residence time, we can write Eq. (20) as

$$\Delta\langle n(d)\rangle = \bar{t}S(d) - G\bar{t}\frac{dn(d)}{dd}$$ (21)

On the left hand side is a readily measureable quantity, as shown for example in Fig. 6, and on the right hand side an average source rate, obtained by averaging Eq. (18). In what follows, that source rate is related to the correct average aggregation rate constant, and efficiency.

4.3. Spatial average efficiency

The in–situ average source term depends on the number densities (that are taken to be independent of position, and so take no part in the averaging process) and the in–situ average aggregation rate constant. The rate constant is given by

$$\beta(d_I,d_{II},r) = \frac{\dot{\gamma}}{6}(d_I + d_{II})^3 \psi(M(d_I,d_{II},r))$$ (22)

It follows that the in–situ average rate constant is

$$\bar{\beta}(d_I,d_{II}) = \frac{(d_I + d_{II})^3}{6}\overline{\dot{\gamma}\psi}$$ (23)

From which we see that the appropriate average efficiency, $\overline{\overline{\psi}}$ for any particle size is the shear–rate weighted in–situ average of the underlying point efficiency.

$$\overline{\overline{\psi}} = \frac{\overline{\dot{\gamma}\psi}}{\overline{\dot{\gamma}}}$$ (24)

Although the development above was conducted specifically for the PFC, this last equation is a quite general statement of the average efficiency to use where there is little spatial variation in the number density. With this definition it is possible to decompose the apparent aggregation rate constant into the product of an average collision rate constant, $\bar{C}$, and an average efficiency, $\overline{\overline{\psi}}$, as though the system were homogeneous:

$$\bar{C}(d_I,d_{II}) = \frac{\overline{\dot{\gamma}}}{6}(d_I + d_{II})^3$$ (25)

$$\bar{\beta}(d_I,d_{II}) = \bar{C}(d_I,d_{II}) \times \overline{\overline{\psi}}(d_I,d_{II})$$ (26)

4.4. An average Mumtaz number

It is convenient to define an apparent average M number using the average shear rate as

$$\overline{\overline{M}} = \frac{\sigma_Y L^* G}{\overline{\dot{\gamma}}^2 \mu d_{eq}^2}$$ (27)

In many cases, M is a proxy for particle size so it is also convenient to group parameters to define a critical aggregate size, D:

$$\overline{\overline{M}} = \left(\frac{D}{d_{eq}}\right)^2$$ (28)

so

$$D = \sqrt{\frac{\sigma_Y L^* G}{\overline{\dot{\gamma}}^2 \mu}}$$ (29)

The critical aggregate size, D, should be understood as the particle size that at the average shear rate has $M=1$, and so disruptive forces are approximately in balance with the strength of growing bridges.

4.5. Calculating the average efficiency from the underlying point values

Returning to the definition of average efficiency, Eq. (24), for the PFC this becomes

$$\overline{\overline{\psi}} = \frac{3}{R^3}\int_0^R r^2\psi(r)\,dr$$ (30)

The dependence of ψ on r arises through the dependence of M on shear rate and since $\dot{\gamma} = 3r/2R\,\bar{\gamma}$, it follows that $M = \overline{\overline{M}}(4/9)(R/r)^2$. With this result it is possible to re–write the integral over M:

$$\overline{\overline{\psi}}(\overline{\overline{M}}) = \frac{4\overline{\overline{M}}^{3/2}}{9}\int_{\frac{4\overline{\overline{M}}}{9}}^\infty M^{-5/2}\psi(M)\,dM$$ (31)

This equation shows how to take the point data of Part I and calculate the average efficiency for use in the PFC. For example, using the Tresca or Tensile failure models produces the results shown in Fig. 7.

Following the approach of Part I, we fit these curves with a sigmoidal curve of the form in Eq. (32), and describe the *location* of the curves by the geometric average of M, $\overline{M}_g$, and the *spread* by the geometric standard deviation, σ_g. The parameters corresponding to Fig. 7 are shown in Table 1.

$$\psi = \begin{cases} \dfrac{1}{1 + (1-\alpha)(M/a)^{-n} + \alpha(M/a)^{-m}} & m > n \\ \dfrac{(1-\alpha)(M/a)^m + \alpha(M/a)^n}{1 + (1-\alpha)(M/a)^m + \alpha(M/a)^n} & m < n \end{cases}$$ (32)

We see that averaging over the PFC both moves the location of the curve (though this is in a sense is arbitrary reflecting the definition of $\overline{\overline{M}}$, Eq. (27)) but also increases the spread – σ_g increasing by approximately 0.6 for both failure models.

It is significant that for both failure models, once averaged, the apparent efficiency scales with the same power of average Mumtaz number, i.e. $m=1.5$, for small values of efficiency, even though
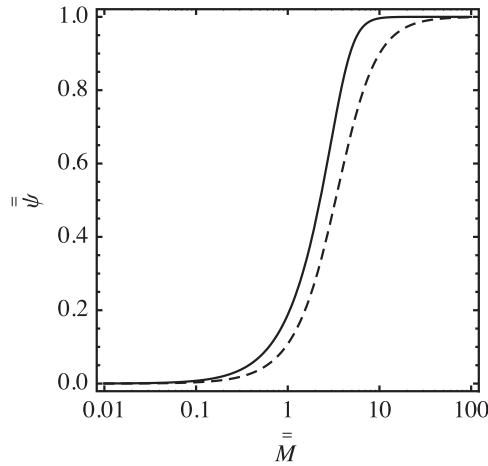
Fig. 7. Aggregation efficiency, averaged across the whole PFC, as a function of the average Mumtaz number for rupture by tensile failure (————), or failure according to Tresca's hypothesis (–––––).

Table 1
Parameters for the dependence of efficiency on Mumtaz number.

Failure mechanism	Point values or PFC averaged	Curve fit to ψ(M)				Properties of ψ (M) or $\overline{\overline{\psi}}\left(\overline{\overline{M}}\right)$	
		a	α	m	n	location $\overline{M}_g$	spread σ_g
Tensile	point: $\psi(M)$	1.779	0.587	2	5	1.66	1.73
	averaged: $\overline{\overline{\psi}}\left(\overline{\overline{M}}\right)$	2.303	0.179	1.5	5	1.92	2.37
Tresca	point: $\psi(M)$	2.576	0.232	4	2	2.74	2.08
	averaged: $\overline{\overline{\psi}}\left(\overline{\overline{M}}\right)$	3.196	0.687	1.5	2	3.17	2.69

for un-averaged, point, values, the scalings are quite different ($m=4$ or 2). This means that model discrimination between the two models is not possible at low efficiencies using averaged values and motivates the search for a method to recover un-averaged results.

4.6. Recovering point efficiencies from measured average efficiencies

The task is to recover $\psi(M)$ from measured values of $\overline{\overline{\psi}}(\overline{\overline{M}})$. Eq. (31) is a Volterra integral equation for $\overline{\overline{\psi}}$ and can be solved by differentiation to give

$$\psi\left(\frac{4}{9}\overline{\overline{M}}\right) = -\frac{2}{3}\overline{\overline{M}}^{5/2}\frac{d}{d\overline{\overline{M}}}\left(\overline{\overline{M}}^{-3/2}\overline{\overline{\psi}}(\overline{\overline{M}})\right)$$

Using Eq. (28) to replace $\overline{\overline{M}}$ with equivalent particle size gives

$$\psi(M) = \frac{1}{3d_{eq}^2}\frac{d}{dd_{eq}}\left(d_{eq}^3\overline{\overline{\psi}}\right) \tag{33}$$

with $M = (4/9)(D/d_{eq})^2$. In other words, point efficiencies can be obtained from the slope of a plot of $d_{eq}^3\overline{\overline{\psi}}$ against d_{eq}.

5. Treating data

5.1. Fitting the model to size distribution data

Eq. (21) allows the calculation of the observed change in mixing-cup size distribution, $\Delta\langle n(d)\rangle$. We do so by first discretising that equation using the approach of Litster et al. (1995) as corrected by Wynn (1996). Two rate constants are needed – the growth rate, G, and the aggregation rate constant, $\overline{\beta}$. The former

can be calculated from the known supersaturation using the results of (Pitt et al., 2012) while the latter is determined as follows. For colliding particles of sizes d_I and d_{II}, calculate

1. the equivalent diameter, d_{eq}, using Eq. (6)
2. the average Mumtaz number, $\overline{\overline{M}}$, from Eq. (28)
3. the average efficiency, $\overline{\overline{\psi}}$, from eq. (32)
4. the average aggregation rate constant, $\overline{\beta}$, from Eq. (26)

In order to achieve this, a fitting exercise is required as the key strength parameters in the Mumtaz number, $\sigma_Y L^*$, are not known. Since particle size is the key independent variable in Fig. 6, it is convenient to fit values for the characteristic size, D, defined in Eq. (29).

In analysing PFC results we have conditions at the inlet and outlet to the capillary. The differential nature of the analysis and change in the PFC means that these conditions are very similar but it is possible to enhance the accuracy of the analysis by treating the right hand side of Eq. (21) as the average of the inlet and outlet conditions. Finally, the nature of the particle-size analyser used here is that it detects particles only down to a size of 2 μm, and appears to be less accurate for high number concentrations of small particles. For these reasons, we chose to fit the model to particle *volume* rather than *number* distributions.

5.2. Selecting a failure model

In fitting to $\Delta\langle n(d)\rangle$ data, an appropriate failure model must be selected – in this work a choice between tension and Tresca. In exploring which of the two was most effective it also became apparent that representing the equivalent diameter by the geometric mean of the colliding particles, i.e. setting $q=1$ often produced a better result. As a consequence, four different candidate models were fitted to the data. The quality of fit obtained can be quantified by the coefficient of determination:

$$R^2 = 1 - \int_0^\infty d^3(\Delta\langle n(d)\rangle - \Delta\langle \hat{n}(d)\rangle)^2 dd / \int_0^\infty d^3\Delta\langle n(d)\rangle^2 dd \tag{34}$$

where $\Delta\langle n(d)\rangle$ are the measured values and $\Delta\langle\hat{n}(d)\rangle$ are those predicted using the best-fit value of D.

In Table 2, results are shown for fitting the four models to 33 sets of experimental data. In 30 occasions of the 33, tension models provide a better fit, with 19 of those corresponding to the case of $q=1$.

This indicates that failure is by tension and that equivalent size is best taken to be the geometric average of colliding particles. As an example, the line in Fig. 6(d) corresponds to a fit of the Tension model, using $q=1$, with $D=10.2\pm0.05$ μm corresponding to $L^*\sigma_Y = 1.88$ Nm^{-1}.

### 5.3. Extracting averaged efficiencies

In discrete form, Eq. (21) becomes a vector of equations with one discrete equation per particle size. If all the terms are known with the exception of spatial average efficiency at each size, it seems possible that each equation could be solved for the efficiency at that size.

Table 2
Results of fitting differing failure models to 33 different sets of data.

	Tension	Tension $q=1$	Tresca	Tresca $q=1$
Average R^2	0.804	0.807	0.739	0.737
Number of cases where fit is best	11	19	3	0
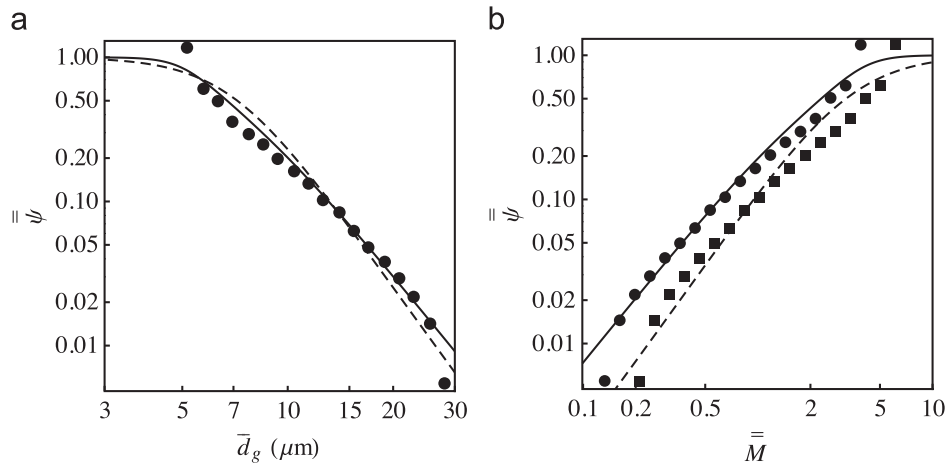
Fig. 8. Values of average efficiency shown as functions of particle size or average Mumtaz number. The lines are Eq. (32) corresponding to tensile failure (————), or failure according to Tresca's hypothesis (——————) using the D values fitted to $\Delta\langle n(d)\rangle$ ie not fitted directly to $\overline{\overline{\psi}}$.
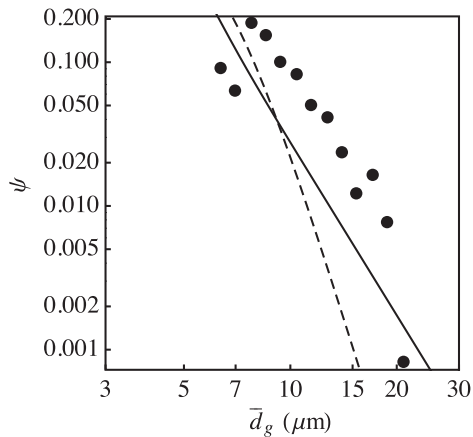
Fig. 9. Point values for efficiency deduced directly from the experimental data. The two lines correspond to the point values deduce theoretically by (Hounslow et al., 2013) using the D values fitted to $\Delta\langle n(d)\rangle$. Legend as in Fig. 7.

The process of extracting efficiencies from size distributions is an inverse problem. In general, the inverse problem of recovering aggregation rate constants from data is irretrievably ill-conditioned (Ramkrishna, 2000), not least because the rate constant is a two-dimensional function of size and the distributions are one-dimensional functions. However in this case, the 2-D nature is provided by Smoluchowski's (known) shear kernel and the aggregation efficiency which, as we have shown, can be reduced to a one-dimensional function of equivalent particle size. The approach we use is to identify a number, typically some tens, of node sizes corresponding to measurement node size and to represent the efficiency function to be determined as an inter-polation between those node sizes; in other words we seek only to determine some tens of values of the efficiency. In this way, it is possible to extract values for average efficiency, $\overline{\overline{\psi}}$, at each of the node sizes as shown for example in Fig. 8. Also shown are the deduced averaged values of efficiency (i.e. those of Fig. 7) using values for D fitted to $\Delta\langle n(d)\rangle$ (and not fitted to the $\overline{\overline{\psi}}$ data). The Tensile model provides a marginally better description.

5.4. Recovering point efficiencies from measured average efficiencies

Values for ψ can be obtained from values for $\overline{\overline{\psi}}$ by means of Eq. (33) provided it is possible to differentiate the $\overline{\overline{\psi}}$ data. In the present case, noise in both measurement of the size distributions and then extraction of $\overline{\overline{\psi}}$ values makes this task difficult. The approach taken was to use the Savitzky-Golay filtering technique (Savitzky and Golay, 1964) which at best gives results of the kind shown in Fig. 9. In this figure the theoretical lines are not fitted to the data, rather they are as calculated in (Hounslow et al., 2013) using the fitted values of D from Fig. 8

Having removed the effects of averaging, it is possible to see that the Tensile model is a better description of the experimental data.

6. Using critical aggregate size, D, to characterise aggregates

Critical aggregate size depends on system properties as described in Eq. (29), which may, in turn, be usefully recast as

$$D^2 = \frac{L^*\sigma_Y G}{\overline{\dot{\gamma}}^2 \mu} = \frac{L^*\sigma_Y}{\mu}\left(\frac{3\pi R^3}{8}\right)^2 \frac{G}{Q^2} \tag{35}$$

In the present work, the right hand side of Eq. (35) is the product of tshree terms: $L^*\sigma_Y/\mu$ are materials properties of the system under study, $(3\pi R^3/8)^2$ is a geometrical property of the PFC and G/Q^2 are (manipulable) experimental operating conditions. In what follows, we report the results of three sets of experiments using rounded seeds, summarised in Table 3. Of the two manipul-able operating conditions, the flow rate, Q, has been directly adjusted while the growth rate, G, has been both directly manipu-lated (by changing inlet supersaturation) and indirectly manipu-lated by changing the seeds loading, w_0, (since higher surface area results in a greater rate of depletion of supersaturation resulting in a reduced average over the whole of the PFC).

6.1. Effect of flow rate

According to Eq. (35), critical aggregate size should be inversely proportional to flow rate. In Fig. 10 that relationship is convin-cingly confirmed. It is notable that the axis intercept is not statistically significantly different from zero.
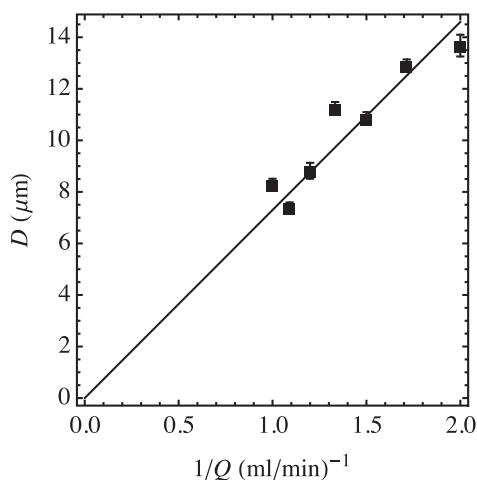
6.2. Effect of supersaturation

According to Eq. (35), the square of critical aggregate size should be directly proportional to crystal growth rate. In Fig. 11 that relationship is convincingly confirmed. Again, it is notable
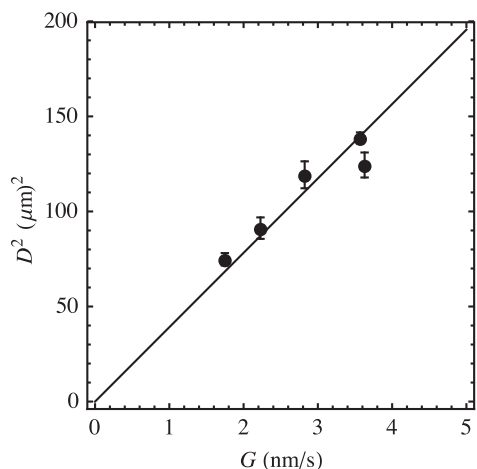
Table 3
Range of conditions for each of three series of experiments using rounded seeds.

Series name	Inlet supersaturation $(S-1)$	Flow rate Q $(ml\,min^{-1})$	Seeds loading w_0 $(kg\,m^{-3})$
"S"	1.65–3.10	0.75	0.42–0.58
"Q"	2.68	0.5–1.0	0.41–0.53
"w_0"	2.68	0.75	0.30–0.90

Fig. 10. The effect of flow rate on critical aggregate size for the "Q" series of data. The line of best fit corresponds to Eq. (35) with $L^*\sigma_Y = 1.25 \pm 0.02\,Nm^{-1}$.
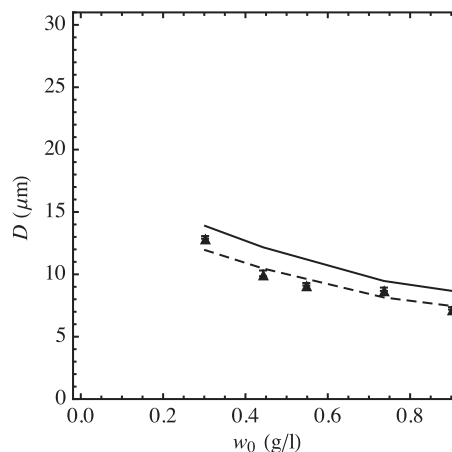

Fig. 11. The effect of inlet supersaturation on critical aggregate size for the "S" set of data. The line of best fit corresponds to Eq. (35) with $L^*\sigma_Y = 1.69 \pm 0.03\,Nm^{-1}$.

Fig. 12. The effect of seeds concentration on critical aggregate size. The lines are predictions based on fits to either the flow rate series of experiments (dashed line) shown in Fig. 10 or the supersaturation series (solid line) shown in Fig. 11.

Fig. 13. Critical aggregate size for all three data series. The line of best fit corresponds to Eq. (35) with $L^*\sigma_Y = 1.35 \pm 0.01\,Nm^{-1}$.

7. Discussion

In this paper we report the development of a PFC capable of automated high quality measurements. The residence time distribution data shown in Figs. 4 and 5 provide compelling evidence that both liquid and solids follow the fluid streamlines and the shear environment that is both inducing and preventing aggregation is uniquely well known.

The concept of the PFC is that it behaves as a differential reactor in which the rate of aggregation varies little along the length of the capillary. There are two components that affect this rate – the concentration of particles and the crystal growth rate, both of which are expected to decrease along the capillary axis. In general this assumption is sufficiently good for the results to be quantitatively sound. We explored a variety of corrections and concluded that the most robust results were obtained by averaging the inlet and outlet size distributions and using the exit growth rate.

The PFC gives data – of the kind shown in Fig. 6d – that show a very clear signature of aggregation.

We have shown how to average point kinetics over a vessel and developed Eq. (24) which is generally applicable to any vessel where solids distribution does not vary significantly with position. In applying this result to the PFC, we introduce an average Mumtaz
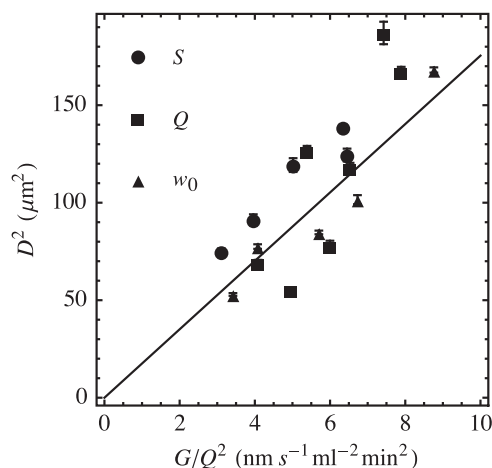
that the axis intercept is not statistically significantly different from zero.

In Fig. 12, the (indirect) effect of seeds loading on critical aggregate size is shown. D decreases as w_0 increases because the average growth rate in the PFC decreases. Also shown in the figure are predictions based on the fits (i.e. the values for $L^*\sigma_Y$) shown in Figs. 10 and 11. Both fits capture the trend well, with that determined from the "Q" series being quantitatively very accurate.

Combining all these results, according to Eq. (35) the square of critical aggregate size should be directly proportional to the ratio of growth rate to flow rate squared. That relationship is confirmed in Fig. 13. Despite some scatter in the data, the slope can be determined with confidence to yield a value for $L^*\sigma_Y$ of $1.35 \pm 0.01\,Nm^{-1}$.

number, $\overline{\overline{M}}$, Eq. (27), and a critical aggregate size, D, Eq. (29). For each run of the PFC, a value of D can be obtained that best describes the measured size distribution.

In Part I we developed a range of models that might describe point aggregation kinetics. We have used two approaches to conclude that a model based on simple tension with a mean size correction factor of $q = 1$ is correct. In the first empirical approach in Table 2, we show that for a substantial set of data failure according to simple tension gives the best fit to the experimental $\Delta\langle n(d)\rangle$ data. In the second approach we use two successive inverse methods to extract first data for efficiency (averaged over the PFC), $\overline{\overline{\psi}}$, as a function of $\overline{\overline{M}}$ (as shown in Fig. 8) and then true point values as shown in Fig. 9. Model discrimination is not possible for averaged data but it appears to be so for point data, where simple tension gives the correct power law scaling. These two approaches offer different strengths and weaknesses. The empirical approach is robust and effective at discrimination, but does not explicitly identify one model as correct; rather it says which works best. By contrast, the inverse approach does explicitly confirm one model, but can only be applied in the near-total absence of noise in the measured data – and so is not robust. That both methods yield the same result leads us to make a firm conclusion.

The purpose of fitting D to a set of data might be understood to be the determination of the material property, $L^*\sigma_Y$, via Eq. (29). The approach we have adopted here is to use that equation to explore – in Fig. 10 to Fig. 13 – whether this is truly a material property (i.e. a constant) and whether D does vary as expected when operating conditions are changed, i.e. that $D^2 \propto G/Q^2$. A variety of estimates for $L^*\sigma_Y$ with rounded COM particles emerge in the range 1–2 Nm^{-1}. The best estimate is shown in Fig. 13 to be $L^*\sigma_Y = 1.35 \pm 0.01$ Nm^{-1}.

In previous work on COM using stirred tanks, (Pitt et al., 2012) showed that their aggregation tendency – $L^*\sigma_Y/M_{50}$ – varied from 0.6 to 1.4. In that result, M_{50} is the value of M (as defined for a stirred tank) for which efficiency is 50%. The value is unknown, should depend only on the spread of shear rates (and not their average) and is expected to be of order 1. On that basis, the result of Pitt et al. is consistent with that presented here.

Two important observations can be made about the quality of the fits in Fig. 10 to Fig. 13. First, the assumption that cementing, i.e. crystal growth, is required for aggregation is confirmed; no additional inter-particle force is available to resist traction due to fluid shear: the axis intercept in all cases is zero. Second, even with a single material – rounded COM in this case – there is more scatter between series of experiments than the model could explain. We return to these two points in Part III of the present series.

8. Conclusions

In Part I of this series we identified three open questions *viz*

- which failure mode is appropriate?
- what value does $L^*\sigma_Y$ take for a given material?
- how should these point kinetics be averaged over a whole vessel?

Each of those has now been answered: failure is best understood to be under simple tension; for rounded particles of COM, $L^*\sigma_Y = 1.35 \pm 0.01$ Nm^{-1}. Finally, for well-mixed vessels averaging is according to Eq. (24).

In Part III of this series, we consider the case of aggregation of growing crystals in the presence of inter-particle forces.

Nomenclature

a	parameter in Eq. (32)
C	collision rate constant (m^3 s^{-1})
d	particle size (m)
d_g	geometric mean size of a pair of colliding particles (m)
D	critical aggregate particle size (m)
f	a function of radial position (various)
F	cumulative residence time distribution (–)
G	crystal growth rate (m s^{-1})
K_{sp}	solubility product (–)
L	length of the PFC capillary (m)
L^*	combined length and angle in the Mumtaz number (m)
m	parameter in Eq. (32)
M	Mumtaz number (–)
n	parameter in Eq. (32)
$n(d, \bullet)$	number density (m^{-4})
q	mean size correction factor (–)
Q	volumetric flow rate (m^3 s^{-1})
r	radial coordinate (m)
r	a rate (m^{-3} s^{-1})
R	capillary radius (m)
S	supersaturation ratio (–)
S	source function (m^{-4} s^{-1})
t	time (s)
t_0	breakthrough time (s)
u	a component of velocity (ms^{-1})
U	centreline axial velocity (ms^{-1})
w_0	feed seeds loading (kg m^{-3})
x	Cartesian coordinate axes
Z	Length of the PFC capillary

Greek letters

α	parameter in Eq. (32)
$\dot{\gamma}$	fluid shear rate (s^{-1})
Δ	a change (out – in)
μ	viscosity (Pa s)
ψ	collision efficiency (–)
σ_Y	yield strength (Pa)

Subscripts

I, II	particles I and II of a colliding pair
Eq	equivalent

Other marks

–	in-situ average
$\langle\rangle$	mixing-cup average
=	apparent average

Refernces

Danckwerts, P.V., 1953. Continuous flow systems: distribution of residence times. Chem. Eng. Sci. 2, 1–13.

Hollander, E.D., Derksen, J.J., Kramer, H.J.M., Van den Akker, H.E.A., 2002. Developing a non-intrusive measuring technique for determining orthokinetic agglomeration rate constants. Meas. Sci. Technol. 13, 807–819.

Hounslow, M., Wynn, E.J.W., Kubo, M., Pitt, K., 2013. Aggregation of growing crystals in suspension: I. Mumtaz revisited. Chem. Eng. Sci. 101, 731–743.

Hounslow, M.J., Mumtaz, H.S., Collier, A.P., Barrick, J.P., Bramley, A.S., 2001. A micromechanical model for the rate of aggregation during precipitation from solution. Chem. Eng. Sci. 56, 2543–2552.

Ilievski, D., Rudman, M., Metcalfe, G., 2001. The separate roles of shear rate and mixing on gibbsite precipitation. Chem. Eng. Sci. 56, 2521–2530.

Litster, J.D., Smit, D.J., Hounslow, M.J., 1995. Adjustable discretized population balance for growth and aggregation. Aiche J. 41, 591–603.

Mumtaz, H.S., Hounslow, M.J., 2000. Aggregation during precipitation from solution: an experimental investigation using Poiseuille flow. Chem. Eng. Sci. 55, 5671–5681.

Pitt, K., Mitchell, G.P., Ray, A., Heywood, B.R., Hounslow, M.J., 2012. Micromechanical model of calcium oxalate monohydrate aggregation in supersaturated solutions: effect of crystal form and seed concentration. J. Cryst. Growth 361, 176–188.

Ramkrishna, D., 2000. Population Balances: Theory and Applications to Particulate Systems in Engineering. Academic Press, San Diego.

Randolph, A.D., Larson, M.A., 1988. Theory of Particulate Processes: Analysis and Techniques of Continuous Crystallization. Academic Press, San Diego.

Savitzky, A., Golay, M.J.E., 1964. Smoothing and differentiation of data by simplified least squares procedures. Anal. Chem. 36, 1627–1639.

Smoluchowski, M., 1917. Versuch einer mathematischen Theorie der Koagulationskinetik kolloider Lösungen. Z. Phys. Chem 92, 9.

Wynn, E.J.W., 1996. Improved accuracy and convergence of discretized population balance of Lister et al. Aiche J. 42, 2084–2086.